INFORME **DFN/RA-05/SP-24**

REF. EXTERNA

# PRODUCTION AND CHARACTERIZATION OF IRRADIATED NUCLEAR FUEL SURROGATES BY DRY POWDER METHOD (IONMAT PROJECT. SUBTASK 1.1)

**DIVISIÓN DE FISIÓN NUCLEAR**

Ciemat Centro de Investigaciones Energéticas, Medioambientales y Tecnológicas

TITULO: Production and characterization of irradiated nuclear fuel surrogates by dry powder method (IONMAT project. Subtask 1.1)

AUTORES: N. Rodríguez-Villagra, J.M. Elorrieta; A. Milena-Pérez; S. Fernández-Carretero; A. Nuñez; L.J. Bonales; L. Gutiérrez; S. Durán; L. Anta; H. Galán

**ABSTRACT:**
Here, a series of Eu-doped (0.02 wt.% $Eu_2O_3$, 0.2 wt.% $Eu_2O_3$, 2 wt.% $Eu_2O_3$) Zr-doped $UO_2$ (20 wt.% $ZrO_2$, 40 wt.% $ZrO_2$, 80 wt.% $ZrO_2$, and 100 wt.% $ZrO_2$) and undoped $UO_2$ pellets, were prepared and characterized. Samples were obtained by pressing the powder mixtures of precursor oxide powders in weighted amounts, and then sintered under reducing atmosphere. A detailed characterization of the pellets was carried out.

| | NOMBRE | FIRMA | FECHA |
|---|---|---|---|
| **Preparado por:** | N. Rodríguez-Villagra | | |
| **Revisado por:** | J.M. Elorrieta | | |
| **Conf por A. C.:** | S. Fernández | | |
| **Aprobado por:** | E.M. González | | |

FECHA DE EMISIÓN

## INDEX


1. INTRODUCTION ..... 5
2. EXPERIMENTAL PROCEDURE. EQUIPMENT AND EXPERIMENTAL TECHNIQUES ..... 9
3. SAMPLES PREPARATION ..... 9
3.1. $UO_2$-$ZrO_2$ pellets ..... 9
3.2. $UO_2$-$Eu_2O_3$ pellets ..... 12
4. EFFECT OF Zr CONTENT ON $UO_2$: CHARACTERIZATION ..... 15
4.1. SEM, GRAIN SIZE AND SPECIFIC SURFACE AREA ..... 16
4.2. XRD ..... 17
4.3. RAMAN SPECTROSCOPY ..... 19
5. EFFECT OF Eu CONTENT ON $UO_2$: CHARACTERIZATION ..... 20
5.1. SEM, GRAIN SIZE AND SPECIFIC SURFACE AREA ..... 21
5.2. XRD ..... 22
5.3. RAMAN SPECTROSCOPY ..... 23
6. CONCLUSIONS ..... 25
7. ACKNOWLEDGEMENTS ..... 26
8. REFERENCES ..... 27

## INDEX OF FIGURES

Figure 1 Schematic representation of the microstructure of SNF pellet and the distribution of FP, and transuranic elements after irradiation in a reactor. Figure taken from Ewing [19] and adapted from [33, 34]....7

Figure 2 Raman spectra of starting $UO_2$ (a) and $ZrO_2$ (b)....10

Figure 3 XRD patterns of starting $UO_2$ (a) and $ZrO_2$ (b), together with their respective reference data. ....11

Figure 4 SEM images of starting powders of a) $UO_2$ and b) $ZrO_2$....11

Figure 5 Raman spectra of starting $UO_2$ (a) and $Eu_2O_3$ (b)....13

Figure 6 XRD patterns of starting $UO_2$ (a) and $Eu_2O_3$ (b), together with their respective reference data. ....14

Figure 7 SEM images of starting powders of a) $UO_2$ and b) $Eu_2O_3$....14

Figure 8 Photographs of the sintered pellets of: a) 100 wt.% $UO_2$, b) $UO_2$ - 20 wt.% $ZrO_2$, c) $UO_2$-40 wt.% $ZrO_2$, d) $UO_2$-80 wt.% $ZrO_2$ and e) 100 wt.% $ZrO_2$....15

Figure 9 SEM images of the prepared samples: a) 100 wt.% $UO_2$, b) $UO_2$ - 20 wt.% $ZrO_2$, c) $UO_2$-40 wt.% $ZrO_2$, d) $UO_2$-80 wt.% $ZrO_2$ and e) 100 wt.% $ZrO_2$....16

Figure 10 Crystal structures of $ZrO_2$ and its transformation with temperature: a) monoclinic ($a \neq b \neq c$; $\alpha=\gamma=90^\circ \neq \beta$), b) tetragonal ($a=b \neq c$; $\alpha=\beta=\gamma=90^\circ$), and c) cubic ($a=b=c$; $\alpha=\beta=\gamma=90^\circ$). (taken from Kongkiatkamon *et al*. [53] and adapted from Sorrentino *et al*. [54]) [55]....17

Figure 11 XRD patterns of the sintered pellets: $UO_2$, $UO_2$ - 20 wt.% $ZrO_2$, $UO_2$-40 wt.% $ZrO_2$, $UO_2$-80 wt.% $ZrO_2$, 100 wt.% $ZrO_2$....18

Figure 12 Raman spectra of the sintered pellets: $UO_2$, $UO_2$ - 20 wt.% $ZrO_2$, $UO_2$-40 wt.% $ZrO_2$, $UO_2$-80 wt.% $ZrO_2$, $ZrO_2$....20

Figure 13 Photographs of the sintered pellets of: a) $UO_2$, b) 0.02 wt.% $Eu_2O_3$ - $UO_2$, c) 0.2 wt.% $Eu_2O_3$ - $UO_2$, and d) 2 wt.% $Eu_2O_3$ - $UO_2$....20

Figure 14 SEM images of the prepared samples: a) $UO_2$, b) 0.02 wt.% $Eu_2O_3$ - $UO_2$, c) 0.2 wt.% $Eu_2O_3$ - $UO_2$, and d) 2 wt.% $Eu_2O_3$ - $UO_2$....21

Figure 15 XRD patterns of the $UO_2$ pellets containing 0 wt.%, 0.02 wt.%, 0.2 wt.% and 2 wt.% $Eu_2O_3$ (a), zoom on the (111) reflection (b), and lattice parameter evolution (c) of the sintered pellets. ....23

Figure 16 Normalized Raman spectra of $UO_2$, $UO_2$-0.02 wt.% $Eu_2O_3$, $UO_2$-0.2 wt.% $Eu_2O_3$, $UO_2$-2 wt.% $Eu_2O_3$....24

## INDEX OF TABLES

Table I Overview of the composition of various cladding Zr-based alloys used commercially in thermal power reactors (taken from [4] and adapted from [5-7]).....5

Table II Methods and techniques used in this project.....9

Table III Raw material characterization of $UO_2$ and $ZrO_2$.....10

Table IV Definition of samples of Zr-doped $UO_2$.....12

Table V Raw material characterization of $UO_2$ and $Eu_2O_3$.....12

Table VI Raman modes characteristic of starting powders used in this work.....13

Table VII Definition of samples of Eu-doped $UO_2$ (*x* in expressed as per-unit atomic).....14

Table VIII Specifications of the as-sintered Zr-doped and undoped $UO_2$ pellets.....15

Table IX Average grain size and SSA of the Zr-doped and undoped $UO_2$ pellets.....16

Table X Lattice parameters and identified phases of the as-sintered Zr-doped and undoped $UO_2$ pellets.....19

Table XI Density values of the as-sintered Eu-doped and undoped $UO_2$ pellets.....21

Table XII Average grain size and SSA of the Eu-doped and undoped $UO_2$ pellets.....22

## 1. INTRODUCTION

A main objective of the High Level Waste Unit (HLWU) of CIEMAT is to reduce uncertainties in Spent Nuclear Fuel (SNF) properties and behaviour in predisposal phase (treatment, conditioning, transport and interim storage) and after disposal closure. Particularly, it aims to understand the most relevant processes driving the chemical evolution of SNF under normal operation and postulated accident scenarios, to identify relevant or typical bounding cases at time of each stage.

The majority of commercial nuclear reactors in the world today are Light Water Reactors (LWRs), either Pressurized Water Reactors (PWRs) or Boiling Water Reactors (BWRs). The nuclear fuel used in these reactors is in the form of $UO_2$ pellets contained in zirconium-based alloy rods [1]. These tubes, known as nuclear fuel cladding, protect the fuel pellets and constitute the first external barrier against the release of Fission Products (FP) into the environment [2], since the first barrier is the own fuel pellet. Zirconium alloys are extensively used for nuclear fuel cladding because of their small neutron absorption cross-section, good resistance to high-temperature corrosion, adequate mechanical properties, and resistance to radiation damage [3]. Table I (taken from [4] and adpated from [5-7]) sums up the cladding alloys that are commercially used and their compositions [5-8].

**Table I Overview of the composition of various cladding Zr-based alloys used commercially in thermal power reactors (taken from [4] and adapted from [5-7]).**

| Alloy | Wt.% | | | | | | Impurities | Structure | Reactor utilization |
|---|---|---|---|---|---|---|---|---|---|
| | Sn | Fe | Cr | Ni | O | Nb | | | |
| Zircaloy-2 | 1.2–1.7 | 0.07–0.2 | 0.05–0.15 | 0.03–0.08 | 0.09–0.16 | – | Hf | Recrystallized | BWR |
| Zircaloy-4 | 1.2–1.7 | 0.18–0.24 | 0.07–0.13 | – | 0.09–0.16 | – | Hf | Cold Work Stress Relieved, Recrystallized | PHWR & PWR |
| ZIRLO | 0.80–1.1 | 0.1 | – | – | 0.105–0.145 | 0.99–1.01 | | Cold Work Stress Relieved | PWR |
| Optimized ZIRLO | 0.67 | 0.1 | – | – | 0.105–0.145 | 1 | | Partially Recrystallized | PWR |
| M5 | – | 0.03–0.05 | 0.015 | – | 0.118–0.148 | 1 | | Recrystallized | PWR |
| E110 | 1 | 0.014 | – | 0.0035 | 0.06 | 1 | | Recrystallized | PWR, RBMK & VVER |

During in-reactor operation, fluctuations (transients) in the reactor power may occur, which are related to radiation effects, thermal expansion, and microstructural alterations, *e.g.* the production of gaseous elements (mainly Xe and Kr) and other FP, concurrently inducing dimensional changes and swelling of the fuel pellet [9, 10]. Particularly, the thermal gradient across the fuel during operation is one of the reasons for the deformation caused in the pellet

and the highly stressed cladding, leading to pellet-clad gap closure (initially filled with inert gas). Pellet-Cladding Interaction (PCI) (general description that takes account of Fuel Cladding Chemical Interaction (FCCI) and Fuel-Cladding Mechanical Interaction (FCMI)), entails a chemical and mechanical interaction between the fuel pellets and their encasing zirconium alloy, and occurs in the majority of commercial fuel rods [10]. This interaction, given through a chemical bonding layer, occurs first at the inter-pellet spaces while a continuing pellet fragmentation (radial and axial cracks) takes place simultaneously [11]. The fuel-cladding interface can be described as composed of two zones, one closer to the cladding (polycrystalline $ZrO_2$) and a second one nearer the fuel, which is mainly formed by solid solutions of $(U,Zr)O_2$ (usually tetragonal or cubic) [12, 13], however few data are available from a structural perspective. Moreover, the occurrence of the PCI phenomenon grows with burn-up, and given the current trend towards increasing burn-up supports the importance of studying PCI. Because PCI might induce cladding fuel failure under certain circumstances [14-16], it is considered a mid-priority phenomenon in the investigation of the safety approach under dry storage [16] that are not currently accounted for in fuel performance codes, partially owing to the absence of data [10, 17, 18]. As a result, understanding the properties of the pellet-clad bonding layers is worthy of study.

After the operation of nuclear fuel in LWR reactor, it results in cracked fuel pellets; production of fission gases (Cs, Rb, Te, I), solid FPs, transuranic elements (*e.g.* Pu, Cm and Am), and activation products; thermal expansion and cladding creep resulting in gap closure; and radioactivity [19-24]. Furthermore, FPs formed during nuclear fuel operation are found as oxide precipitates and solid solutions, and as metallic inclusions (ε-particles), among others (Figure 1). The physico-chemical properties of the irradiated fuel also get considerably modified [19, 22, 23] as a function of time and radial position. Among the FPs, the rare earth elements (REE) form a substantial fraction; and particularly, around 4-20 wt.% of light REE corresponds to two lanthanides (Ln), europium and gadolinium [25]. REE are typically present as solid solutions within the uranium oxide fuel matrix, due to their capacity to substitute U atoms in the lattice [26-28]. The knowledge of the influence of FPs on SNF integrity is relevant for the physico-chemical processes involved in the pre-disposal and final disposal stages. After discharge from the reactor, the spent fuel is stored in pools at the reactor site to allow for the residual heat removal and decay of the very short-lived nuclides. Subsequently, the fuel is transferred to wet or dry interim storage. Interim storage solutions

for SNF are needed regardless of the fuel cycle strategy. The long-term integrity of SNF is almost ensured; however, the likely lifetime extension programs of such storage facilities should include ageing and degradation studies to demonstrate safe long-term performance, including that of undetected damaged fuel [29, 30]. Here, we initiate our studies by addressing the Eu as a solely dopant, because its average ionic radius from lanthanides [31]. The combined influence of Gd and Eu will be further investigated. The solid solubility of $Eu_2O_3$ in $UO_2$ and defect chemistry have been studied and reported in the literature [26, 27, 32].

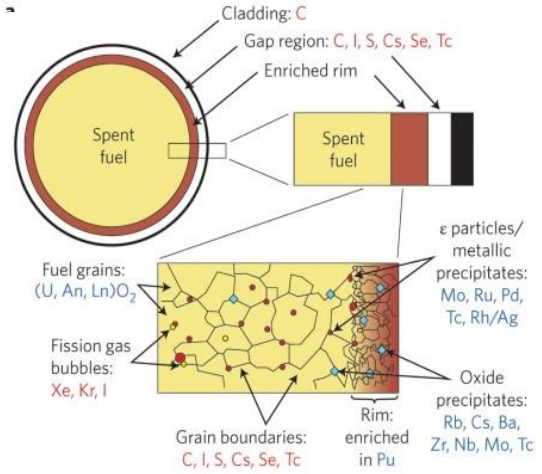


**Figure 1 Schematic representation of the microstructure of SNF pellet and the distribution of FP, and transuranic elements after irradiation in a reactor. Figure taken from Ewing [19] and adapted from [33, 34].**

The experimental work with SNF is a challenging matter, inherently difficult and expensive because of its radiological constraints and requirements, added to its physico-chemical complexity that can steadily change with time (Figure 1) [19, 21, 33-35]. The SNF is one of the most complex materials in terms of chemical composition in different phases and states. A deep understanding of complex phenomena occurring in this material is a requirement for building predictive models including all back-end stages at short, medium and long-time scales in safety assessments of SNF. The above-mentioned constraints and the fact that U is essentially the main element present in SNF matrix (in the form of $UO_2$) are consequently motivation for research of surrogate $UO_2$-based systems (using non-irradiated nuclear fuel

and model U-based materials) that can show some of the important behaviours of the irradiated fuel. Knowing that working with SNF is more representative of the realistic scenario, the results are complicated to interpret and make a full understanding of the systems difficult. To gain knowledge on separate and synergic effects and also to conduct fundamental research, the use of non-irradiated alternatives is important before carrying out experimentation on real irradiated systems presenting radiological risks that must be handled with particular care (in hot-cells which capability is limited to some countries). Therefore, it is necessary to produce suitable non-radioactive analogues that closely resemble nuclear fuel in terms of crystallography and microstructure so that we can better understand how changes in the sample surface affect it.

One of the specific goals of IONMAT project, carried out at the HLWU, is the fabrication and characterization of SNF surrogates, with physico-chemical features similar to those reported for irradiated nuclear fuel at medium and high burn-ups, including microstructural and mechanical characterization. It includes from traditional procedures followed in industry (dry route) to advanced techniques (wet route). In particular, task 1.1 aims to mimic some chemical composition of SNF through the manufacturing of irradiated nuclear fuel surrogates by dry powder method. To this end, and based on the above mentioned details, “model materials” that represent some physico-chemical properties maintaining a certain degree of conservatism are obtained and examined in detail. Particularly, we focused on $UO_2$-$Eu_2O_3$ and $UO_2$-$ZrO_2$ pellets:

The specific objectives of subtask 1.1 are:

1. Sintering conditions:
    - Sintering atmosphere: reducing (4.7%$H_2$/$N_2$).
    - Sintering temperature/time: 1675°C for 4 h.
    - Pressing pressures (uniaxial): 700 MPa
2. Effect of dopant content
    - Tetravalent Zr(IV) as $ZrO_2$: 0-100 wt.%.
    - Trivalent Eu(III) as $Eu_2O_3$: 0-2 wt.%.

## 2. EXPERIMENTAL PROCEDURE. EQUIPMENT AND EXPERIMENTAL TECHNIQUES

For the accomplishment of the objectives, the methods/techniques listed in Table II were used.

**Table II Methods and techniques used in this project.**

| Technique | Parameter | Equipment |
|---|---|---|
| BET | $N_2$-BET Surface Area<br>V abs ($N_2$, $cm^3 \cdot g^{-1}$) vs $P/P_0$ | ASAP 2020 (Micromeritics)<br>ISO 12800E |
| XRD | Identification of major and minor single or multiple phases / Structure determination<br>Intensity vs diffraction angle<br>Lattice parameters<br>Quantification of phase mixtures | D8 ADVANCE Eco (Bruker) – ICDD<br>Cu Kα radiation (λ=1.54056 Å), 40 kV and 25 mA<br>Bragg-Brentano configuration geometry Software EVA&TOPAS (Bruker Analytical X-Ray Systems) |
| Raman spectroscopy | Structural / speciation<br>Characteristic spectrum (“fingerprint”)<br>Intensity vs frequency (Δν incident-scattered) | LabRam HR Evolution (HORIBA)<br>He-Ne laser with wavelength=632.8 nm. |
| SEM-EDX | Surface morphology/grain size/Elemental identification (quantification)<br>Lineal intercept method (Heyn)<br>Scattered electrons from the surface.<br>(I vs ev) | TM4000 Plus 15 kV (HITACHI)<br>ASTM E 112-96 ;UNE-EN ISO 643:2012 |
| Laser diffraction | Particle size distribution | Malvern Particle Analyser 2600<br>Malvern Mastersizer 3000 Hydro EV and Aero S |
| Archimedean method | Density | Sartorious kit |
| Furnace | 1700°C, atmosphere control | Termolab |
| Polisher | | Vector LC250 (Buehler) |
| Mixer Mill | Max. frequency of 30 Hz | MM 400 (Retsch) |
| Uniaxial Press | 25 T | C256C (Power team, Johannesburg, South Africa) |

## 3. SAMPLES PREPARATION

### 3.1. $UO_2$-$ZrO_2$ PELLETS

A series of $ZrO_2$-doped and undoped $UO_2$ pellets ($UO_2$, $UO_2$-20 wt.% $ZrO_2$, $UO_2$-40 wt.% $ZrO_2$, $UO_2$-80 wt.% $ZrO_2$ and pure $ZrO_2$) were manufactured. in this case, zirconium oxide of 99.98 % purity (Alfa Aesar) and natural uranium dioxide [36] were the powders used for preparing the samples. These raw powders were characterized in terms of the

Specific Surface Area (SSA) by BET method with $N_2$ and the mean particle size by Laser Diffraction. The results of this characterization can be seen in Table III.

**Table III Raw material characterization of $UO_2$ and $ZrO_2$.**

| Material | SSA (BET) ($m^2 \cdot g^{-1}$) | Average particle size (µm) | Lattice parameter (nm) | Space group |
|---|---|---|---|---|
| $UO_2$ | 3.75 ± 0.04 | 3.68 ± 0.06 | a = b = c = 0.547120 (13) | Cubic, $Fm\bar{3}m$ |
| $ZrO_2$ | 6.41 ± 0.03 | 2.02 ± 0.01 | a = 0.514594(5); b = 0.521081(4); c = 0.531393(5); α = γ = 90°; β = 99.2084(2) | Monoclinic, P1 21/c 1 |

Starting powders were also measured by XRD, Raman spectroscopy and SEM.

Raman spectrum of $UO_2$ powder (Figure 2 at left) shows the well-known features of slightly-hyperstoichiometric uranium dioxide: a) the triply degenerate $T_{2g}$ mode at 445 $cm^{-1}$; b) the lattice-distortion-related LO phonon mode at about 570 $cm^{-1}$; c) the band at ~630 $cm^{-1}$ associated with oxygen-sublattice defects provoked by the excess of oxygen atoms; and d) the first overtone of the LO mode (2LO) centered at about 1140 $cm^{-1}$ [37-39]. In addition, $ZrO_2$ spectrum (Figure 2 at right) shows the typical bands and features described in the literature for this compound with the monoclinic structure [40].

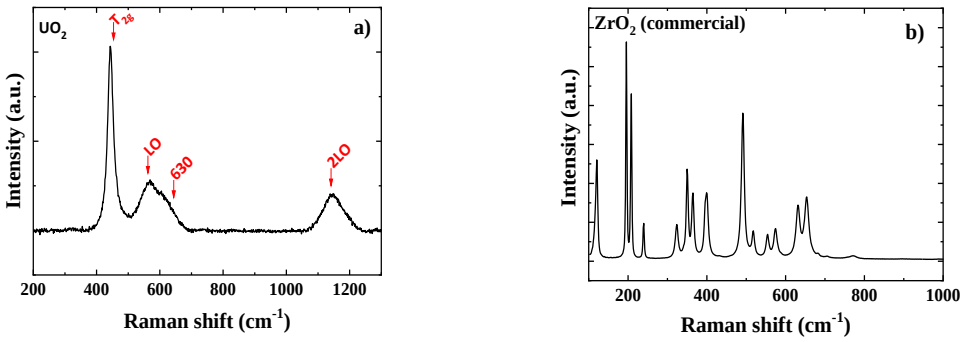


**Figure 2 Raman spectra of starting $UO_2$ (a) and $ZrO_2$ (b).**

XRD patterns of the $UO_2$ and $ZrO_2$ starting powders were acquired and compared with their corresponding reference data, thus confirming the purity of these materials (see Figure 3). The obtained lattice parameters are given in Table III. The XRD analysis indicates the structure of $UO_2$ is fluorite-type phase and monoclinic for $ZrO_2$ (m-$ZrO_2$).

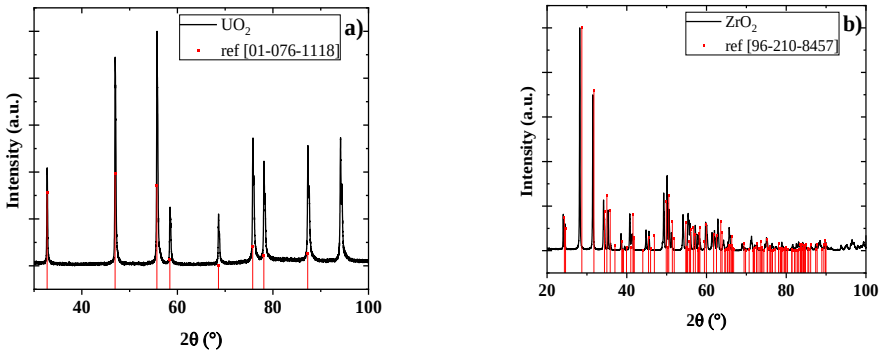


**Figure 3 XRD patterns of starting $UO_2$ (a) and $ZrO_2$ (b), together with their respective reference data.**

Finally, SEM images were also acquired from each starting powder. A representative example of each one is shown inFigure 4.

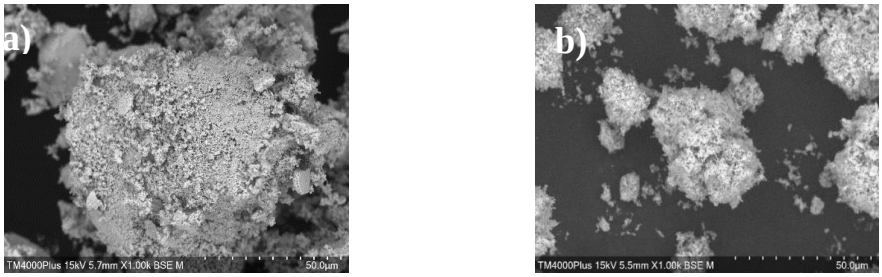


**Figure 4 SEM images of starting powders of a) $UO_2$ and b) $ZrO_2$.**

The procedure through which the target pellets were fabricated consisted of mechanical dry blending of the ceramic powders (together with the binder EBS (Ethylene bis stearamide), where the powders were homogenized together with the binder in a mill-homogenizer at 15 Hz for 15 minutes, followed by cold compaction at 700 MPa (uniaxial press) to obtain green pellets. The latter were then calcined at three temperature steps (100, 300, and 500 °C) and sintered at 1675 °C for 4 h (5ºC·min$^{-1}$). Both treatments were conducted under a reducing atmosphere (4.7%$H_2/N_2$) –to avoid $UO_2$ oxidation – in an alumina tubular furnace. Finally, polishing and thermal annealing were carried out to reveal grains (10 minutes at 1590ºC under a 4.7% $H_2$-$N_2$ atmosphere). This fabrication process has been previously tested in our laboratory [41]. Table IV shows the samples fabricated by this pathway.

**Table IV Definition of samples of Zr-doped $UO_2$.**

| Labelled Material | $ZrO_2$ added (ppm) |
|---|---|
| $UO_2$ | 0 |
| $UO_2$-20 wt.% $ZrO_2$ | 200 |
| $UO_2$-40 wt.% $ZrO_2$ | 400 |
| $UO_2$-80 wt.% $ZrO_2$ | 800 |
| 100 wt.% $ZrO_2$ | - |

### 3.2. $UO_2$-$Eu_2O_3$ PELLETS

A series of undoped and Eu-doped $UO_2$ pellets ($UO_2$, $UO_2$-0.02 wt.% $Eu_2O_3$, $UO_2$-0.2 wt.% $Eu_2O_3$ and $UO_2$-2 wt.% $Eu_2O_3$) were manufactured by pressing mixtures of precursor oxide powders in weighted quantities. Europium oxide (99.99 %, Aldrich) and natural $UO_2$ [36] were the powders used for preparing the samples. The $Eu_2O_3$ commercial reagent was initially thermally treated at 1000 ºC in air for its dehydration.

Before the samples sintering, raw powders were characterized in terms of the Specific Surface Area (SSA) by BET with by $N_2$ adsorption [42] and the mean particle size by Laser Diffraction. The results of this characterization can be seen in Table V.

**Table V Raw material characterization of $UO_2$ and $Eu_2O_3$.**

| Material | SSA (BET) ($m^2 \cdot g^{-1}$) | Average particle size (µm) | Lattice parameter (nm) | Space group |
|---|---|---|---|---|
| $UO_2$ | 3.75 ± 0.04 | 3.68 ± 0.06 | a = b = c = 0.547093 (1) | Cubic, $Fm\bar{3}m$ |
| $Eu_2O_3$ | 6.72 ± 0.03 | 5.85 ± 0.10 | a = b = c = 1.087040 (3) | Cubic, $Ia\bar{3}$ |

Starting powders were also measured by Raman spectroscopy, XRD and SEM. Raman spectrum of $UO_2$ powder (Figure 5 at left) shows the formerly explained features. In addition, $Eu_2O_3$ spectrum (Figure 5 at right) shows the typical bands and features described in the literature for this compound [43-45]. The absence of $Eu(OH)_3$ characteristic Raman vibration modes at 302.5, 377.4, and 384.8 $cm^{-1}$ [46, 47], which are generally found as a mixed phase, suggests that the calcined $Eu_2O_3$ is of a high purity. The corresponding Raman shifts and modes assignments of both powder materials are shown in Table VI.

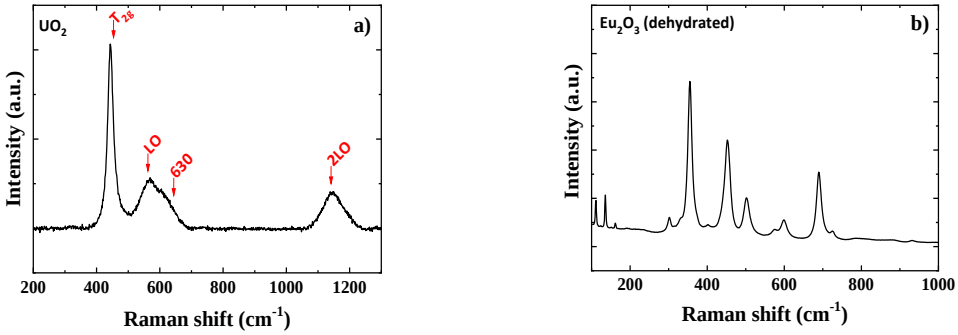


**Figure 5 Raman spectra of starting $UO_2$ (a) and $Eu_2O_3$ (b).**

**Table VI Raman modes characteristic of starting powders used in this work.**

| **Raman shifts for $UO_2$ ($cm^{-1}$) by other authors [38, 39]** | **Raman mode assigned ($UO_2$) [38, 39]** |
|---|---|
| 445 | $T_{2g}$ |
| 575 | LO phonon |
| 1150 | 2LO phonon |
| **Raman shifts for $Eu_2O_3$ ($cm^{-1}$) by other authors [48]** | **Raman mode assigned ($Eu_2O_3$) [48]** |
| 91.5 | $F_g$ |
| 116.6 | $A_g$ |
| 132.9 | $F_g$ |
| 142.7 | $E_g$ |
| 176.0 | $F_g$ |
| 284.3 | $F_g + E_g$ |
| 315.6 | $A_g$ |
| 338.5 | $F_g$ |
| 385.6 | $A_g$ |
| 425.9 | $F_g$ |
| 566.1 | $F_g$ |

XRD patterns of the $UO_2$ and $Eu_2O_3$ starting powders were acquired and compared with their corresponding reference data, thus confirming the purity of these materials (see Figure 6). The obtained lattice parameters are given in Table V.

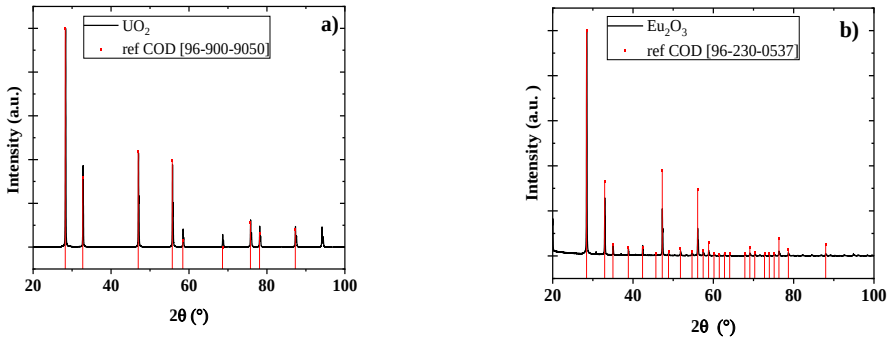


**Figure 6 XRD patterns of starting $UO_2$ (a) and $Eu_2O_3$ (b), together with their respective reference data.**

Finally, SEM images were also acquired from each starting powder. A representative example of each one is shown in Figure 7.

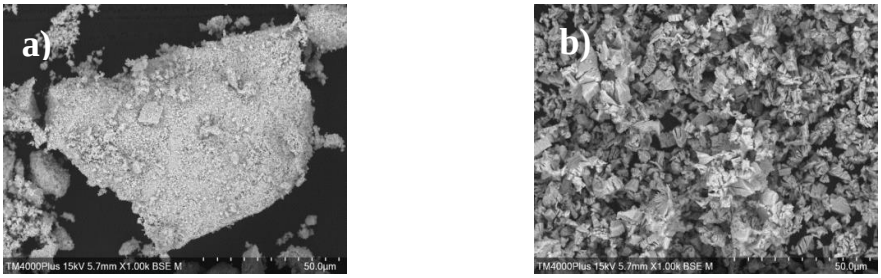


**Figure 7 SEM images of starting powders of a) $UO_2$ and b) $Eu_2O_3$.**

The pellets were fabricated by conventional ceramic processing with the same sequential steps as the previous section (see section 3.2).

Once sintered, a detailed characterization of the pellets was carried out. Table VII shows the samples fabricated by this pathway.

**Table VII Definition of samples of Eu-doped $UO_2$ (*x* in expressed as per-unit atomic).**

| Labelled Material | $Eu_2O_3$ added (ppm) | x in $U_{1-x}Eu_xO_2$ |
|---|---|---|
| $UO_2$ | 0 | 0.00000 |
| $UO_2$-0.02 wt.% $Eu_2O_3$ | 200 | 0.00031 |
| $UO_2$-0.2 wt.% $Eu_2O_3$ | 2000 | 0.00307 |
| $UO_2$-2 wt.% $Eu_2O_3$ | 20000 | 0.03037 |

## 4. EFFECT OF Zr CONTENT ON $UO_2$: CHARACTERIZATION

Likewise, the effect of zirconium on the sintered pellets will be studied in the following sections. The characteristics of the as-sintered undoped and Zr-doped $UO_2$ pellets (Figure 8) are given in Table VIII.

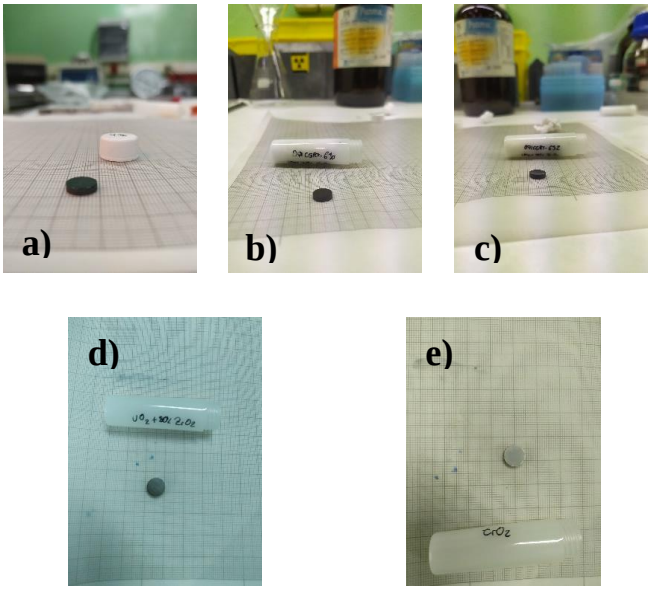


**Figure 8 Photographs of the sintered pellets of: a) 100 wt.% $UO_2$, b) $UO_2$ - 20 wt.% $ZrO_2$, c) $UO_2$-40 wt.% $ZrO_2$, d) $UO_2$-80 wt.% $ZrO_2$ and e) 100 wt.% $ZrO_2$.**

The bulk density of the pellet was measured by the general water immersion Archimedean method. The density values were calculated and showed in Table VIII, using mean plus one standard deviation (± 1σ), on a several measurements (between four and twelve). The average bulk density decreased from the undoped $UO_2$ pellet (9.1 g·cm$^{-3}$) with increasing $ZrO_2$ content in the $UO_2$ sintered pellets, as expected.

**Table VIII Specifications of the as-sintered Zr-doped and undoped $UO_2$ pellets.**

| SAMPLE | $UO_2$ | 20 wt.% $ZrO_2$ - $UO_2$ | 40 wt.% $ZrO_2$ - $UO_2$ | 80 wt.% $ZrO_2$ - $UO_2$ | 100 wt.% $ZrO_2$ |
|---|---|---|---|---|---|
| **Density immersion (g·cm$^{-3}$)** | 9.1 ± 0.1 | 8.6 ± 0.1 | 8.1 ± 0.1 | 6.1 ± 0.6 | 5.5 ± 0.3 |
| **Density geom. (g·cm$^{-3}$)** | 9.6 ± 0.3 | 8.5 ± 0.1 | 8.0 ± 1.0 | 5.7 ± 0.1 | 5.1 ± 0.1 |

## 4.1. SEM, GRAIN SIZE AND SPECIFIC SURFACE AREA

The morphology of the pellets surface was examined by SEM, revealing a non-homogeneous grain structure for the highest dopant amounts (Figure 9). As the composition becomes richer in $ZrO_2$, small grains located between the matrix grains start to appear, probably due to $ZrO_2$-rich particles [49] and once the solubility of $ZrO_2$ in cubic $UO_2$ is achieved. Representative images shown in Figure 9 were used for the calculation of grain size (

Table IX). The average grain sizes of the undoped and $ZrO_2$-doped $UO_2$ pellets are in the range 5 – 7.6 µm and again, all the SSA values are in the same order of magnitude, around 0.3 $m^2 \cdot g^{-1}$.

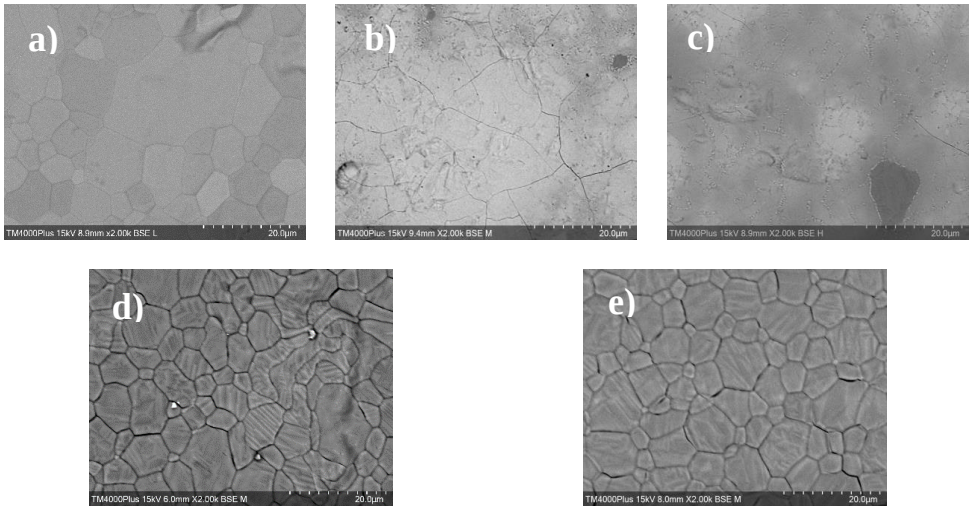


**Figure 9 SEM images of the prepared samples: a) 100 wt.% $UO_2$, b) $UO_2$ - 20 wt.% $ZrO_2$, c) $UO_2$-40 wt.% $ZrO_2$, d) $UO_2$-80 wt.% $ZrO_2$ and e) 100 wt.% $ZrO_2$.**

**Table IX Average grain size and SSA of the Zr-doped and undoped $UO_2$ pellets.**

| SAMPLE | $UO_2$ | 20 wt.% $ZrO_2$ - $UO_2$ | 40 wt.% $ZrO_2$ - $UO_2$ | 80 wt.% $ZrO_2$ - $UO_2$ | $ZrO_2$ |
|---|---|---|---|---|---|
| **Grain size (µm)** | 7.6 ± 0.6 | 5 ± 2 | 5.2 ± 0.4 | 7.1 ± 0.5 | 5.8 ± 0.6 |
| **SSA ($m^2 \cdot g^{-1}$)** | 0.28 ± 0.01 | 0.3 ± 0.01 | 0.32 ± 0.02 | 0.30 ± 0.01 | 0.35 ± 0.01 |

### 4.2. XRD

To study the lattice parameter evolution of the $UO_2$ pellets due to the presence of zirconium, XRD patterns were acquired under the same conditions (Figure 11) and the corresponding lattice parameters were obtained by Rietveld refinement (Table X). It is known that the crystal structure of $UO_2$ is cubic, fluorite-type, so the lattice is characterized by only one lattice parameter (*a*). Pure $ZrO_2$ under atmospheric pressure shows three thermodynamically stable polymorphs depending on temperature: monoclinic (m-$ZrO_2$), tetragonal (t-$ZrO_2$) and cubic (c-$ZrO_2$) structures (Figure 10) [49-51]. Generally, m-$ZrO_2$ is the stable form of $ZrO_2$ at low temperature [49, 50]. As shown in Figure 10, there is a transition to a tetragonal structure [50] around 1170 ˚C and exist up to around 2300 ˚C [50, 51]. Then, there is a controversy about the existence of c-$ZrO_2$ allotropic form at greater than 2370 °C [52], or it could reach its melting temperature (around 2700 ˚C) [50].

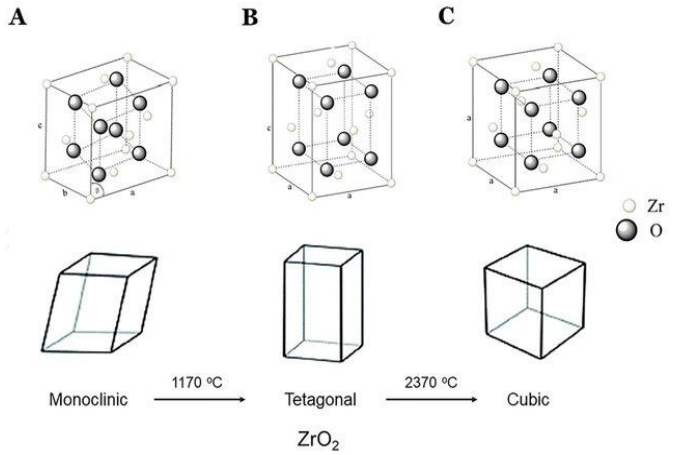


**Figure 10 Crystal structures of $ZrO_2$ and its transformation with temperature: a) monoclinic (a≠b≠c; α=γ=90˚≠β), b) tetragonal (a=b≠c; α=β=γ=90˚), and c) cubic (a=b=c; α=β=γ=90˚). (taken from Kongkiatkamon *et al*. [53] and adapted from Sorrentino *et al.* [54]) [55].**

The XRD patterns of the undoped $UO_2$ or $ZrO_2$, and $ZrO_2$-doped sintered pellets (Figure 11) show that the main peak positions shift to higher angles with increasing $ZrO_2$ content up to 40 wt.% of $ZrO_2$, indicating that the lattice contracts when Zr(IV) is incorporated into the $UO_2$ lattice substituting U(IV) atoms, as stated in the literature [56]. After the mixture composition, the cubic fluorite structure of $UO_2$ is lost and then, the existence of

polymorphic forms of pure $ZrO_2$, whose main phases are found in the form of tetragonal and monoclinic (Table X).

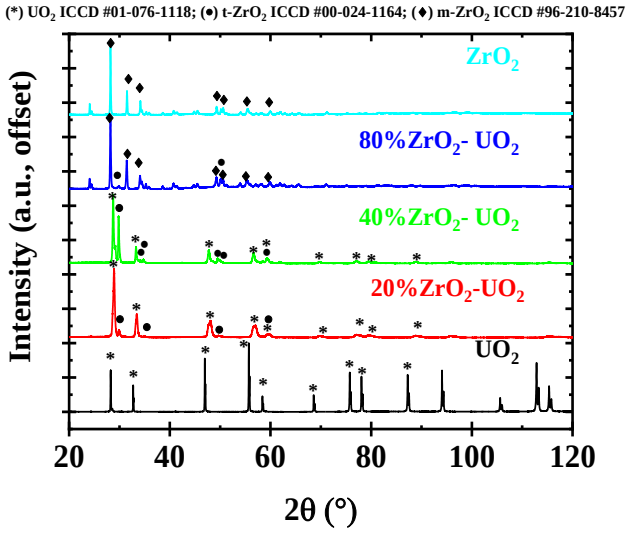


**Figure 11 XRD patterns of the sintered pellets: $UO_2$, $UO_2$ - 20 wt.% $ZrO_2$, $UO_2$-40 wt.% $ZrO_2$, $UO_2$-80 wt.% $ZrO_2$, 100 wt.% $ZrO_2$.**

$ZrO_2$ found in the PCI layers closer to the fuel has been shown to be either cubic or tetragonally stabilised at room temperature [10, 13, 57-59]. The t-$ZrO_2$ phase seems to be gradually replaced by c-$ZrO_2$ as burnup increases [60]. A combination of factors including radiation damage, FPs dopants, accommodation of U in solid solution and others are the cause of this stabilization of both the cubic and tetragonal phases in nuclear fuel [10, 13]. Consequently, the addition of $ZrO_2$ to $UO_2$ shows polymorphic transformations in $ZrO_2$ because of changes in crystal lattice from the monoclinic phase, observed in pure $ZrO_2$. Urania-zirconia solid solutions have been previously studied by Cohen *et al.* [49], who prepared a range of $(U,Zr)O_2$ solid solutions by dry powder route at 1725-1750 ˚C in $H_2$(g) for 72-110 h. They observed the following: (i) Below 1660 ˚C, there is a "miscibility gap" with a sharp decrease of the $ZrO_2$ solubility in $UO_2$ (from around 5 to 20 wt.% $ZrO_2$ and also 60 wt.% $ZrO_2$); (ii) a two-phase region of cubic and tetragonal at 1600-2300 ˚C. At 1690 ˚C, the solubility limit is in the range of 30 – 60 wt.% $ZrO_2$, however it is around 30 wt% $ZrO_2$ at 1875 ˚C; (iii) stabilization of a cubic solid solution in the temperature range 2366 to 2556 ˚C.

The decreased solubility of $UO_2$ in tetragonal and monoclinic $ZrO_2$ [49] in the sample doped with 80 wt.% $ZrO_2$ may induce segregated $UO_2$. Then, according to these data and under our sintering conditions, a conservative estimation for the solubility limit in this case would therefore be around 30 – 60 wt.% $ZrO_2$.

**Table X Lattice parameters and identified phases of the as-sintered Zr-doped and undoped $UO_2$ pellets.**

| SAMPLE | $UO_2$ | 20 wt.% $ZrO_2$ - $UO_2$ | 40 wt.% $ZrO_2$ - $UO_2$ | 80 wt.% $ZrO_2$ - $UO_2$ | 100 wt.% $ZrO_2$ |
|---|---|---|---|---|---|
| **Lattice param. (nm)** | 100% $UO_2$ *Fm-3m*<br>a=b=c= 0. 5470(2) | 92% $U_{1-y}Zr_yO_2$<br>(y = 0.48) *Fm-3m*<br>a=b=c= 0.5403 (1)<br>< 8% $ZrO_2$ SG P *42/nmc*<br>a=0.3686(2)<br>b=0.3686(2)<br>c= 0.5138(3) | 67% $U_{0.5}Zr_{0.5}O_2$<br>*Fm-3m*<br>a=b=c= 0.5404(1)<br>33% t-$ZrO_2$ SG P *42/nmc*<br>a=0.3688(4)<br>b=0.3688(4)<br>c= 0.5150(1) | 91% $U_{1-x}Zr_xO_2$<br>(x = 0.04) *P1 21/c1*<br>a=0.5161(2);<br>b=0.5214 (2);<br>c= 0.5324(2)<br>4% t-$ZrO_2$ SG P *42/nmc*<br>a=0.3660;<br>b=0.3660;<br>c= 0.5206 (8)<br>~3% $U_{1-y}Zr_yO_2$<br>(y = 0.5) *Fm-3m*<br>a=b=c= 0.5461(9)<br>2% $UO_2$ *Fm-3m*<br>a=b=c= 0. 5471(2) | 100% m-$ZrO_2$<br>*P1 21/c1*<br>a=0.5156(3)<br>b=0.5211(1)<br>c= 0.5324(7) |

## 4.3. RAMAN SPECTROSCOPY

Figure 12 shows the Raman spectra of the as-prepared undoped $UO_2$ and $ZrO_2$-doped samples. Raman spectrum of undoped $UO_2$ shows the typical fingerprint of this compound, already described in section 3.1. As the theoretical U/Zr ratio decreases, it induces changes in the Raman spectra, such as the $T_{2g}$, LO and 2LO bands broadening and their shift towards higher wavenumber (up to 40 wt.% $ZrO_2$), which indicates that Zr has been incorporated into the $UO_2$ lattice, and an increase of local disorder is taking place [84]. Conversely, for the sample doped with 80 wt.% $ZrO_2$ several peaks centred at 183, 301, 335, 381, 476, 536, 559, 613, and 636 $cm^{-1}$ appear, which correspond to a dominant monoclinic phase of $ZrO_2$ [61]. This confirms that at 40 wt.% $ZrO_2$ we are still within the solubility range, but not at 80 wt.% $ZrO_2$.

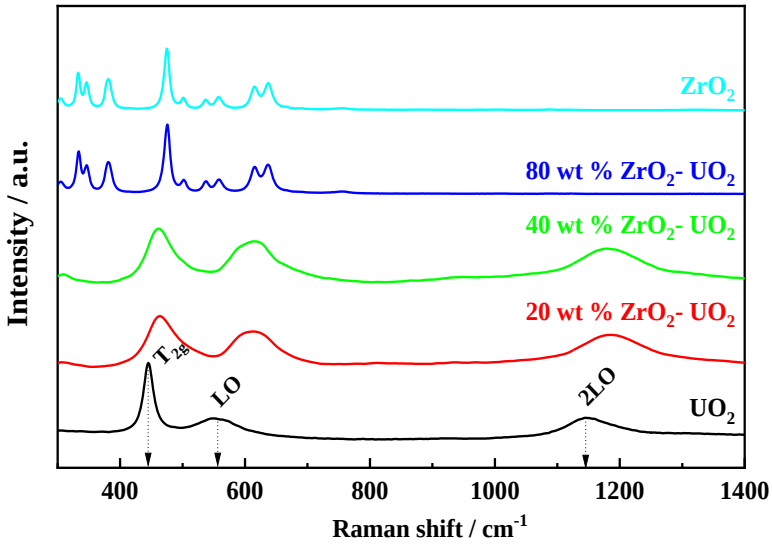


**Figure 12 Raman spectra of the sintered pellets: $UO_2$, $UO_2$ - 20 wt.% $ZrO_2$, $UO_2$-40 wt.% $ZrO_2$, $UO_2$-80 wt.% $ZrO_2$, $ZrO_2$.**

## 5. EFFECT OF Eu CONTENT ON $UO_2$: CHARACTERIZATION

In the following sections, the effect of europium on $UO_2$ sintered pellets using the above-mentioned techniques will be studied. An overview of the density values obtained for the as-sintered Eu-doped and undoped $UO_2$ pellets (Figure 13) is given in Table XI.

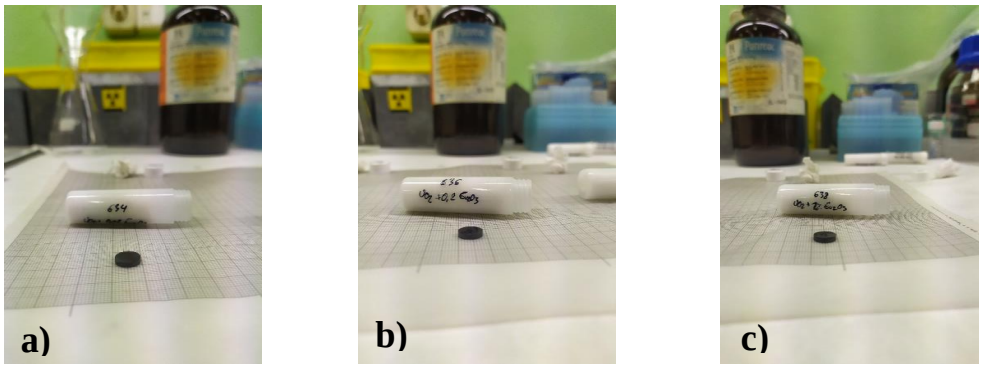


**Figure 13 Photographs of the sintered pellets of: a) $UO_2$, b) 0.02 wt.% $Eu_2O_3$ - $UO_2$, c) 0.2 wt.% $Eu_2O_3$ - $UO_2$, and d) 2 wt.% $Eu_2O_3$ - $UO_2$.**

The bulk density of the pellet was measured by the general water immersion Archimedean method. The density values were calculated and showed in Table XI, using mean plus one standard deviation (± 1σ), on a several measurements (between four and twelve). The average bulk density decreased from the undoped $UO_2$ pellet (9.8 g·cm$^{-3}$) with increasing $Eu_2O_3$ content in the $UO_2$ sintered pellets, as expected.

**Table XI Density values of the as-sintered Eu-doped and undoped $UO_2$ pellets.**

| SAMPLE | $UO_2$ | 0.02 wt.% $Eu_2O_3$-$UO_2$ | 0.2 wt.% $Eu_2O_3$-$UO_2$ | 2 wt.% $Eu_2O_3$-$UO_2$ |
|---|---|---|---|---|
| **Density immersion (g·cm$^{-3}$)** | 9.8 ± 0.1 | 9.6 ± 0.1 | 9.3 ± 0.2 | 9.3 ± 0.8 |
| **Density geom. (g·cm$^{-3}$)** | 9.6 ± 0.3 | 10.0 ± 0.7 | 9.7 ± 0.1 | 9.8 ± 0.3 |

## 5.1. SEM, GRAIN SIZE AND SPECIFIC SURFACE AREA

Representative SEM images are shown in Figure 14, revealing a uniform grain structure related to a solid solution, and isolated porosity. This might confirm the phase homogeneity in the pellets through the studied compositions.

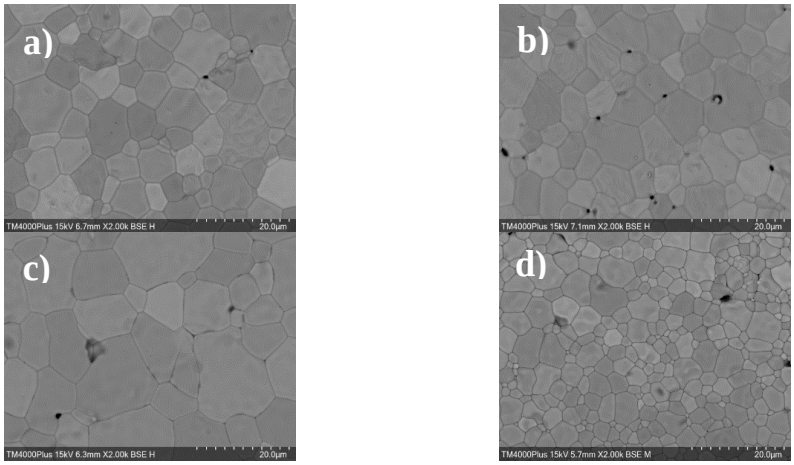


**Figure 14 SEM images of the prepared samples: a) $UO_2$, b) 0.02 wt.% $Eu_2O_3$ - $UO_2$, c) 0.2 wt.% $Eu_2O_3$ - $UO_2$, and d) 2 wt.% $Eu_2O_3$ - $UO_2$.**

From these images, the average grain size of the different samples was estimated via the linear intercept method [62, 63]. These results are depicted in Table XII. The grain size of the pellets doped with 0.02 wt.% $Eu_2O_3$ remains unchanged with regard to undoped $UO_2$; however, this value increases a little for the 0.2 wt.% $Eu_2O_3$ doped sample and then it

decreases for the highest dopant amount, *i.e.* 2 wt.% $Eu_2O_3$. The corresponding results of the SSA (BET, $N_2$) are all in the same order of magnitude.

**Table XII Average grain size and SSA of the Eu-doped and undoped $UO_2$ pellets.**

| SAMPLE | $UO_2$ | 0.02 wt.% $Eu_2O_3$-$UO_2$ | 0.2 wt.% $Eu_2O_3$-$UO_2$ | 2 wt.% $Eu_2O_3$-$UO_2$ |
|---|---|---|---|---|
| **Grain size (µm)** | 6.9 ± 0.8 | 6.7 ± 0.5 | 11.0 ± 1.0 | 5.000 ± 1.0 |
| **SSA ($m^2 \cdot g^{-1}$)** | 0.43 ± 0.01 | 0.55 ± 0.02 | 0.26 ± 0.01 | 0.21 ± 0.01 |

## 5.2. XRD

To study the lattice parameter evolution of the $UO_2$ pellets due to the presence of europium, XRD patterns were acquired under the same conditions and the corresponding lattice parameters were obtained by Rietveld refinement (Figure 15). As it has been formerly shown, crystalline structure of $UO_2$ is cubic fluorite-type structure characterized by only one lattice parameter (*a*). The patterns of $UO_2$ pellets containing 0.02 wt.%, 0.2 wt.% and 2 wt.% $Eu_2O_3$ also correspond to a fluorite-type structure (Figure 15.a), meaning that they conform a $(U,Eu)O_2$ solid solution, which is in agreement with the literature [28, 64, 65]. No segregated $Eu_2O_3$ is observed in any of the samples, implying that the dopant is well dissolved into $UO_2$ grains, as already suggested by the SEM images. Comparison of XRD patterns of the undoped material with Eu-doped samples indicates that the presence of increasing content of Eu additive does not affect the crystalline structure significantly. There is a shift to higher 2θ values with increasing $Eu_2O_3$ concentration, observed in the 28.2º doublet (see the steady shift in (111) reflection in Figure 15.b), indicating that the lattice parameter of the doped sample is smaller than the undoped $UO_2$, and the higher the concentration of dopant is, the lower lattice parameter value (Figure 15.c) [65].

In particular, it shows a linear decrease (Vegard's law ) with increasing Eu content, similar to what has been previously observed in this kind of samples [65] and when $UO_2$ is doped with other trivalent elements [66, 67]. In the selected range of *x* in $U_{1-x}Eu_xO_2$ (between 0 and 3.04 mol%, see Table VII), $Eu_2O_3$ content ≤ 2 wt.%, the solubility limit is not reached (around 60 – 65 mol% [64]). Vegard´s law-like behavior has been confirmed to be valid only in the region where a complete solid solution is established [68], as in this case. Therefore, a regression analysis was performed on the measured lattice parameters of Eu-doped $UO_2$ solid solution, which can be expressed as:

$$\mathbf{a} = (\mathbf{0.54713} \pm \mathbf{2.33 \cdot 10^{-6}}) + (-\mathbf{0.01225} \pm \mathbf{2.4 \cdot 10^{-4}}) \cdot \mathbf{x} \qquad (1)$$

where *a* is the lattice parameter in nm, and *x* is the Eu content in $UO_2$. The coefficients of eq. *(1)* are determined by using a least-squares method where the relative coefficient is 0.99922.

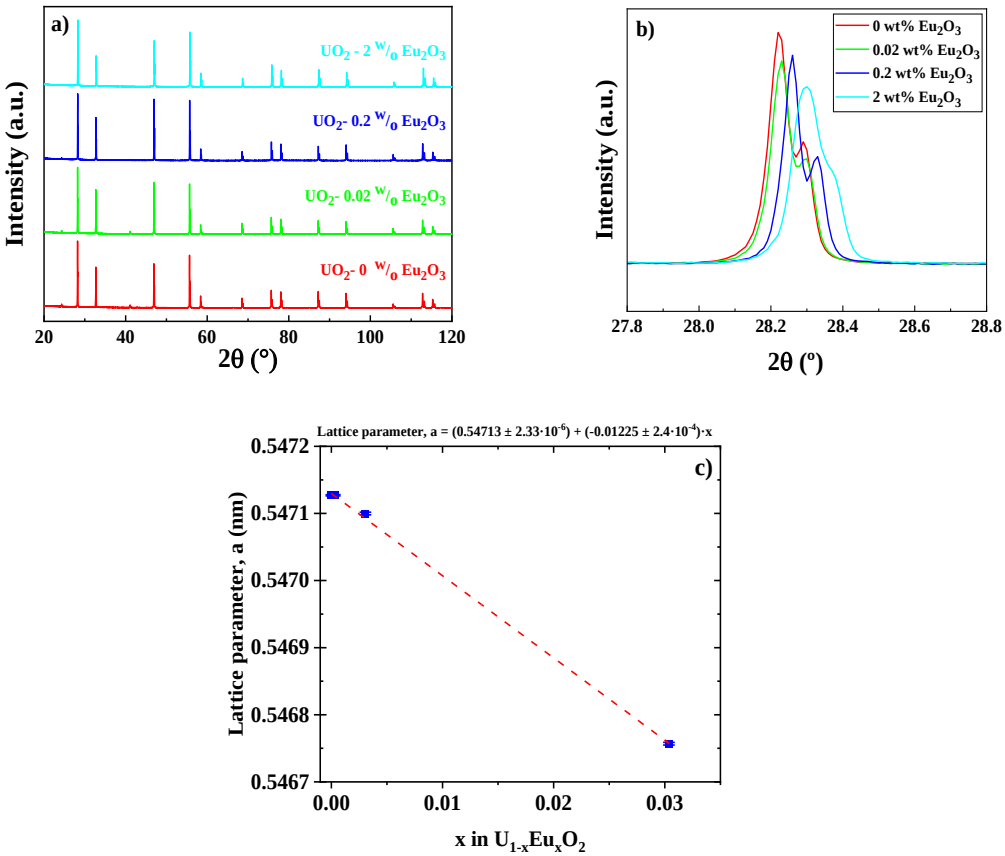


**Figure 15 XRD patterns of the $UO_2$ pellets containing 0 wt.%, 0.02 wt.%, 0.2 wt.% and 2 wt.% $Eu_2O_3$ (a), zoom on the (111) reflection (b), and lattice parameter evolution (c) of the sintered pellets.**

## 5.3. RAMAN SPECTROSCOPY

It has been recognised that Raman spectroscopy is capable of distinguishing defects of the O sublattice in $UO_2$ [67, 69-71], thus, a Raman analysis could allow us to identify oxygen vacancies (due to $Eu^{3+}$ incorporation) present in each of the prepared Eu-doped samples. The acquired Raman spectra on the undoped $UO_2$ and Eu-doped samples are shown

in Figure 16. All of them reveal the main features of the typical fingerprint of $UO_2$ fluorite structure (see section 3.1).

The broad feature at 500 - 650 $cm^{-1}$, mainly formed in this case by the peak centered at ~530 $cm^{-1}$ (marked with an arrow in Figure 10), can be interpreted as a "defects band" due to oxygen-vacancy-induced lattice distortion associated with the presence of trivalent cations. The intensity of this peak remains low at 0 and 0.02 wt.% $Eu_2O_3$, but it noticeably increases with increasing Eu loading, as shown in similar cases like Gd-, Nd- and La-doped $UO_2$ [67, 69, 72] for similar doping level. The other band featured in that region, at ~575 $cm^{-1}$ (LO mode), is related to structure distortions and, as expected, it behaves equivalently to that at ~530 $cm^{-1}$. This behaviour can be interpreted as due to $Eu_2O_3$ incorporation into the cubic lattice of $UO_2$, which also agrees with XRD results. The intensity of the 2LO band at ~1050 $cm^{-1}$ is retained at 0-0.2 wt.% $Eu_2O_3$, but significantly decreases at 2 wt.%, as a result of the distortion of the fluorite lattice structure induced by doping. These observations are consistent with those of Lee *et al.* [67] and Talip *et al.* [69] who observed similar results analyzing Gd- and La -doped $UO_2$ samples, *i.e.* an intensity decrease of the 2LO band when increasing the La or Gd content, respectively.

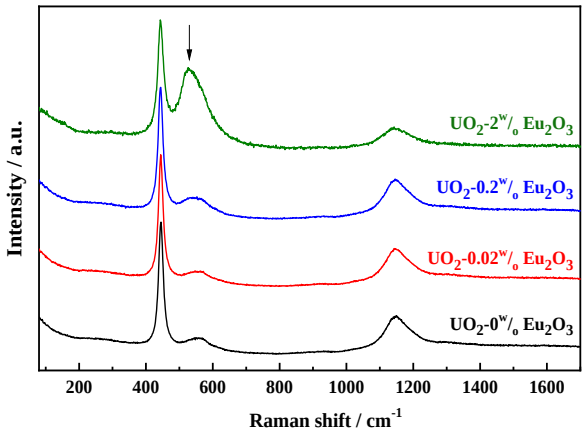


**Figure 16 Normalized Raman spectra of $UO_2$, $UO_2$-0.02 wt.% $Eu_2O_3$, $UO_2$-0.2 wt.% $Eu_2O_3$, $UO_2$-2 wt.% $Eu_2O_3$.**

## 6. CONCLUSIONS

Mixtures of $ZrO_2$-doped $UO_2$, in a wide range of likely compositions within the PCI layer that simulates the $ZrO_2/UO_2$ bonding (chemical adhesion) in HBU fuels, *i.e.* the PCI phenomenon, and undoped $UO_2$ have been obtained and characterized. Regarding the fabrication of these surrogate samples via "dry powder route", it is a complex process and it is susceptible of inducing segregated $ZrO_2$ phases (depending on the solubility limit) and polymorphism of $ZrO_2$ in samples depending on the sintering conditions.

Preliminary results indicate that the "dry powder route" route seems to be relatively acceptable for the obtained samples. Work is currently underway to produce Zr-doped $UO_2$ via "wet route" using advanced fabrication techniques from the co-precipitation of zirconyl and uranyl stock solutions followed by pressing and sintering, that will need to be characterized in terms of crystal structure, oxygen-to-metal ratio, and impurity content. The aim is to compare the samples microstructure with that from dry route.

Additionally, a series of $UO_2$ pellets doped with different amounts of $Eu_2O_3$ (0–2 wt.%) have been sintered by "dry powder" route, and analyzed by SEM, BET, XRD and Raman. In agreement with prior studies, our XRD data reveal that an increase in Ln dopant concentration produces a contraction of the fluorite structure possibly due to the joint effects of smaller cation size of Eu and shorter U/Eu-O bonds and/or hypo-stoichiometry [73], shown by the refined lattice parameters. Raman spectroscopy confirmed the presence of oxygen vacancies in the structure as a consequence of Eu doping, demonstrated by increasing intensity of the so-called "defects band" with Eu concentration.

## 7. ACKNOWLEDGEMENTS

This research is part of the project of R+D+i PID2021-124913OA-I00, IONMAT project funded by MICIU/AEI/10.13039/501100011033/, Proyectos de Generación de Conocimiento 2021. Authors also want to thank the funding for this research from the European Commission Horizon 2020 Research and Training Programme of the European Atomic Energy Community (EURATOM) (H2020-NFRP-2016-2017-1) under grant agreement n° 847593 (EURAD project).

## 8. REFERENCES


[1] IAEA, Thermophysical Properties of Materials for Nuclear Engineering: A Tutorial and Collection of Data. Vienna: International Atomic Energy Agency, 2009.

[2] A. T. Motta, A. Couet, and R. J. Comstock, "Corrosion of Zirconium Alloys Used for Nuclear Fuel Cladding", *Annual Review of Materials Research*, vol. 45, pp. 311-343, 2015.

[3] U. Stoll and N. Slavinskaya, "Corrosion behavior of zirconium alloys in the aqueous environment. Phenomenological aspects. Overview", *Journal of Nuclear Science and Technology*, vol. 60, pp. 573-602, 2023.

[4] M. H. A. Piro, D. Sunderland, S. Livingstone, *et al.*, "2.09 - Pellet-Clad Interaction Behavior in Zirconium Alloy Fuel Cladding", in *Comprehensive Nuclear Materials (Second Edition)*, R. J. M. Konings and R. E. Stoller, Eds., ed Oxford: Elsevier, 2020, pp. 248-306.

[5] B. Cox, F. Garzarolli, and P. Rudling, "Corrosion of Zr-Nb Alloys. ZIRAT-9 Special Topic.", Advanced Nuclear Technology International, Sweden, 2004.

[6] R. B. Rebak, "The Long-Term Environmental Degradation of Zirconium Alloys in Contact With Spent Nuclear Fuel: A Review", in *ASME 2008 Pressure Vessels and Piping Conference*, 2008, pp. 209-214.

[7] T. Alam, M. K. Khan, M. Pathak, *et al.*, "A review on the clad failure studies", *Nuclear Engineering and Design*, vol. 241, pp. 3658-3677, 2011.

[8] K. Komuro, "Welding of zirconium alloys", *Welding International*, vol. 8, pp. 141-148, 1994.

[9] C. Ciszak, L. Desgranges, P. Garcia, *et al.*, "On the origins and the evolution of the fuel-cladding bonding phenomenon in PWR fuel rods", *Journal of Nuclear Materials*, vol. 520, pp. 110-120, 2019.

[10] D. G. Frost, C. O. T. Galvin, M. W. D. Cooper, *et al.*, "Thermophysical properties of urania-zirconia $(U,Zr)O_2$ mixed oxides by molecular dynamics", *Journal of Nuclear Materials*, vol. 528, p. 151876, 2020.

[11] J. T. A. Roberts, Structural Materials in Nuclear Power Systems: Springer New York, NY, 1981.

[12] C. Gibert, "Influence de l'irradiation et de la présence de lithium sur la nature cristallographique de la zircone dans le cadre de l'étude de la corrosion du zircaloy 4 en milieu réacteur à eau pressurisée," Châtenay-Malabry, Ecole centrale de Paris, 1998.

[13] K. Nogita and K. Une, "Formation of Pellet-Cladding Bonding Layer in High Burnup BWR Fuels", *Journal of Nuclear Science and Technology*, vol. 34, pp. 679-686, 1997.

[14] IAEA, Review of Fuel Failures in Water Cooled Reactors vol. No. NF-T-2.1. Vienna, 2010.

[15] J. B. Minne, "Contribution à la modélisation du couplage mécanique-chimique de l'évolution de l'interface pastille-gaine sous irradiation," Laboratoire Interdisciplinaire Carnot de Bourgogne École Doctorale Carnot-Pasteur, Université de Bourgogne, 2013.

[16] OCDE/NEA, Pellet-clad Interaction in Water Reactor Fuels : Seminar Proceedings. Aix-en-Provence, France, 9-11 March 2004.: OCDE, Paris, 2005.

[17] G. Rossiter, "Development of the ENIGMA fuel performance code for whole core analysis and dry storage assessments", *Nuclear Engineering and Technology*, vol. 43, pp. 489-498, 2011.

[18] J. D. Hales, R. L. Williamson, S. R. Novascone, *et al.*, "BISON theory manual the equations behind nuclear fuel analysis", Idaho National Lab.(INL), Idaho Falls, ID (United States), 2016.

[19] R. C. Ewing, "Long-term storage of spent nuclear fuel", *Nat Mater*, vol. 14, pp. 252-257, 2015.

[20] B. Kienzler and H. Geckeis, "Radioactive wastes and disposal options", *EPJ Web Conf.*, vol. 189, p. 00014, 2018.

[21] C. Corkhill and N. Hyatt. (2018). *Nuclear Waste Management*. Available: https://dx.doi.org/10.1088/978-0-7503-1638-5

[22] J. Bruno, L. Duro, and F. Diaz-Maurin, "13 - Spent nuclear fuel and disposal", in *Advances in Nuclear Fuel Chemistry*, M. H. A. Piro, Ed., ed: Woodhead Publishing, 2020, pp. 527-553.

[23] K. Spahiu, "State of the Knowledge Report - Spent Nuclear Fuel Domain 3.1.1. EURAD - European Joint Programme on Radioactive Waste Management (847593)", 2021.

[24] S. Caruso, E. Vlassopoulos, R. Dagan, *et al.*, "EURAD project Deliverable 8.1: State-of-the-art report. Work Package 8", NAGRA, 2022.

[25] S. Bourg and C. Poinssot, "Could spent nuclear fuel be considered as a non-conventional mine of critical raw materials?", *Progress in Nuclear Energy*, vol. 94, pp. 222-228, 2017.

[26] T. Ohmichi, S. Fukushima, A. Maeda, *et al.*, "On the relation between lattice parameter and O/M ratio for uranium dioxide-trivalent rare earth oxide solid solution", *Journal of Nuclear Materials*, vol. 102, pp. 40-46, 1981.

[27] K. Park and D. R. Olander, "Defect models for the oxygen potentials of gadolinium-and europium-doped urania", *Journal of Nuclear Materials*, vol. 187, pp. 89-96, 1992.

[28] R. Venkata Krishnan, G. Jogeswararao, G. Panneerselvam, *et al.*, "Solid solubility and thermal expansion studies of uranium–europium mixed oxides", *Journal of Nuclear Materials*, vol. 465, pp. 719-723, 2015.

[29] P. Mcconnell, B. Hanson, M. Lee, *et al.*, "Extended dry storage of used nuclear fuel: Technical issues: A USA perspective", *Nuclear Engineering and Technology*, vol. 43, pp. 405-412, 2011.

[30] OCDE/NEA, "The Safety of Long-Term Interim Storage Facilities in NEA Member Countries", 2017.

[31] S. K. Potts, P. Kegler, G. Modolo, *et al.*, "Structural incorporation of europium into uranium oxides", *MRS Advances*, vol. 8, pp. 278-284, 2023.

[32] T. Fujino, K. Ouchi, Y. Mozumi, *et al.*, "Composition and oxygen potential of cubic fluorite-type solid solution EuyU1−yO2+x (x ≧ 0) and rhombohedral Eu6UO12+x' (x'< 0)", *Journal of Nuclear Materials*, vol. 174, pp. 92-101, 1990.

[33] D. W. Shoesmith, "Fuel corrosion processes under waste disposal conditions", *Journal of Nuclear Materials*, vol. 282, pp. 1-31, 2000.

[34] E. C. Buck, B. D. Hanson, and B. K. McNamara, "The geochemical behaviour of Tc, Np and Pu in spent nuclear fuel in an oxidizing environment", *Geological Society, London, Special Publications,* vol. 236, pp. 65-88, 2004.

[35] H. Charlton, G. Baldinozzi, and M. Patel, "A review of the oxygen vacancy ordering in surrogate structures simulating Pu-based nuclear ceramics", *Frontiers in Nuclear Engineering,* vol. 1, 2023.

[36] A. Milena-Pérez, N. Rodríguez-Villagra, S. Fernández-Carretero, *et al.*, "Thermal air oxidation of $UO_2$: Joint effect of precursor's nature and particle size distribution", *Progress in Nuclear Energy,* vol. 159, p. 104629, 2023.

[37] T. Livneh and E. Sterer, "Effect of pressure on the resonant multiphonon Raman scattering in $UO_2$", *Physical Review B,* vol. 73, p. 085118, 2006.

[38] H. He and D. Shoesmith, "Raman spectroscopic studies of defect structures and phase transition in hyper-stoichiometric $UO_{2+x}$", *Physical Chemistry Chemical Physics,* vol. 12, pp. 8109-8118, 2010.

[39] J. M. Elorrieta, L. J. Bonales, N. Rodriguez-Villagra, *et al.*, "A detailed Raman and X-ray study of $UO_{2+x}$ oxides and related structure transitions", *Physical Chemistry Chemical Physics,* vol. 18, pp. 28209-28216, 2016.

[40] S. N. Basahel, T. T. Ali, M. Mokhtar, *et al.*, "Influence of crystal structure of nanosized ZrO2 on photocatalytic degradation of methyl orange", *Nanoscale Research Letters,* vol. 10, p. 73, 2015.

[41] S. Fernandez, M. I. Nieto, J. Cobos, *et al.*, "$CeO_2$ pellet fabrication as spent fuel matrix analogue", *Journal of the European Ceramic Society,* vol. 36, pp. 3505–3512, 2016.

[42] S. Brunauer, P. Emmet, and E. Teller, "Adsorption of Gases in Multimolecular Layers", *Journal of the American Chemical Society,* vol. 60, p. 309, 1938.

[43] L. A. Tucker, F. J. Carney, P. McMillan, *et al.*, "Raman and Resonance Raman Spectroscopy of Selected Rare-Earth Sesquioxides", *Applied Spectroscopy,* vol. 38, pp. 857-860, 1984.

[44] J. Yu, L. Cui, H. He, *et al.*, "Raman spectra of $RE_2O_3$ (RE=Eu, Gd, Dy, Ho, Er, Tm, Yb, Lu, Sc and Y): laser-excited luminescence and trace impurity analysis", *Journal of Rare Earths,* vol. 32, pp. 1-4, 2014.

[45] M. V. Abrashev, N. D. Todorov, and J. Geshev, "Raman spectra of $R_2O_3$ (R—rare earth) sesquioxides with C-type bixbyite crystal structure: A comparative study", *Journal of Applied Physics,* vol. 116, 2014.

[46] M. Y. Yang, D. Huang, P. H. Hao, *et al.*, "Study of the Raman peak shift and the linewidth of light-emitting porous silicon", *Journal of Applied Physics,* vol. 75, pp. 651-653, 1994.

[47] J.-G. Kang, Y. Jung, B.-K. Min, *et al.*, "Full characterization of $Eu(OH)_3$ and $Eu_2O_3$ nanorods", *Applied Surface Science,* vol. 314, pp. 158-165, 2014.

[48] S. Jiang, J. Zhang, and S. Yan, "Shear stress induced phase transitions of cubic $Eu_2O_3$ under non-hydrostatic pressures", *AIP Advances,* vol. 13, 2023.

[49] I. Cohen and R. M. Berman, "A metallographic and X-ray study of the limits of oxygen solubility in the $UO_2$-$ThO_2$ system", *Journal of Nuclear Materials,* vol. 18, pp. 77-107, 1966.

[50] R. Terki, G. Bertrand, H. Aourag, *et al.*, "Structural and electronic properties of zirconia phases: A FP-LAPW investigations", *Materials Science in Semiconductor Processing*, vol. 9, pp. 1006-1013, 2006.

[51] A. Arafati, E. Borhani, S. M. S. Nourbakhsh, *et al.*, "Synthesis and characterization of tetragonal / monoclinic mixed phases nanozirconia powders", *Ceramics International*, vol. 45, pp. 12975-12982, 2019.

[52] S. Kumar, S. Bhunia, and A. K. Ojha, "Effect of calcination temperature on phase transformation, structural and optical properties of sol–gel derived $ZrO_2$ nanostructures", *Physica E: Low-dimensional Systems and Nanostructures*, vol. 66, pp. 74-80, 2015.

[53] S. Kongkiatkamon, D. Rokaya, S. Kengtanyakich, *et al.*, "Current classification of zirconia in dentistry: an updated review", *PeerJ 11:e15669*, 2023.

[54] R. Sorrentino, C. O. Navarra, R. Di Lenarda, *et al.*, "Effects of Finish Line Design and Fatigue Cyclic Loading on Phase Transformation of Zirconia Dental Ceramics: A Qualitative Micro-Raman Spectroscopic Analysis", *Materials*, vol. 12, p. 863, 2019.

[55] Y. Han and J. Zhu, "Surface Science Studies on the Zirconia-Based Model Catalysts", *Topics in Catalysis*, vol. 56, pp. 1525-1541, 2013.

[56] H. Xiao, X. Wang, C. Long, *et al.*, "Investigation of the mechanical properties of ZrO2-doped UO2 ceramic pellets by indentation technique", *Journal of Nuclear Materials*, vol. 509, pp. 482-487, 2018.

[57] R. M. Berman, "Homogenization of two-phase mixtures of $ZrO_2$-$UO_2$ by irradiation", *Journal of Nuclear Materials*, vol. 17, pp. 313-323, 1965.

[58] L.-G. Liu, "New high pressure phases of $ZrO_2$ and $HfO_2$", *Journal of Physics and Chemistry of Solids*, vol. 41, pp. 331-334, 1980.

[59] S. Van den Berghe, A. Leenaers, B. Vos, *et al.*, Observation of a pellet-cladding bonding layer in high-power fuel. Nuclear Energy Agency of the OECD (NEA): Organisation for Economic Co-Operation and Development - Nuclear Energy Agency, 2005.

[60] K.-T. Kim, "$UO_2$/Zry-4 chemical interaction layers for intact and leak PWR fuel rods", *Journal of Nuclear Materials*, vol. 404, pp. 128-137, 2010.

[61] C. Ciszak, M. Mermoux, S. Miro, *et al.*, "Micro-Raman analysis of the fuel-cladding interface in a high burnup PWR fuel rod", *Journal of Nuclear Materials*, vol. 495, pp. 392-404, 2017.

[62] K. W. Kang, J. H. Yang, J. H. Kim, *et al.*, "Improvement of $UO_2$ Pellet Properties by Controlling the Powder Morphology of Recycled $U_3O_8$ Powder", *Journal of Nuclear Science and Technology*, vol. 45, pp. 1150-1154, 2008.

[63] ISO, "ISO/FDIS 643:2012 Steels-Micrographic determination of the apparent grain size", ed, 2012.

[64] R. Venkata Krishnan, R. Babu, A. Senapati, *et al.*, "Thermophysical properties of uranium–europium mixed oxides", *Journal of Advanced Ceramics*, vol. 4, pp. 253-259, 2015.

[65] E. K. Papynov, O. O. Shichalin, I. Y. Buravlev, *et al.*, "$UO_2$-$Eu_2O_3$ compound fuel fabrication via spark plasma sintering", *Journal of Alloys and Compounds*, vol. 854, p. 155904, 2021.

[66] K. Iwasaki, T. Matsui, K. Yanai, *et al.*, "Effect of Gd2 O3 Dispersion on the Thermal Conductivity of UO2", *Journal of Nuclear Science and Technology*, vol. 46, pp. 673-676, 2009.

[67] J. Lee, J. Kim, Y.-S. Youn, *et al.*, "Raman study on structure of $U_{1-y}Gd_yO_{2-x}$ (y=0.005, 0.01, 0.03, 0.05 and 0.1) solid solutions", *Journal of Nuclear Materials*, vol. 486, pp. 216-221, 2017.

[68] M. M. Bućko, "Ionic conductivity of $CaO–Y_2O_3–ZrO_2$ materials with constant oxygen vacancy concentration", *Journal of the European Ceramic Society*, vol. 24, pp. 1305-1308, 2004.

[69] Z. Talip, T. Wiss, P. E. Raison, *et al.*, "Raman and X-ray Studies of Uranium–Lanthanum-Mixed Oxides Before and After Air Oxidation", *Journal of the American Ceramic Society*, vol. 98, pp. 2278-2285, 2015.

[70] J. M. Elorrieta, L. J. Bonales, S. Fernández, *et al.*, "Pre-and post-oxidation Raman analysis of $(U, Ce)O_2$ oxides", *Journal of Nuclear Materials*, vol. 508, pp. 116-122, 2018.

[71] A. Milena-Pérez, L. J. Bonales, N. Rodríguez-Villagra, *et al.*, "Raman spectroscopy coupled to principal component analysis for studying $UO_2$ nuclear fuels with different grain sizes due to the chromia addition", *Journal of Nuclear Materials*, vol. 543, p. 152581, 2021.

[72] J. Lee, J. Kim, Y.-S. Youn, *et al.*, "Surface characterization of (U,Nd)O2: the influence of trivalent-dopant on structure of UO2", *Progress in Nuclear Science and Technology*, vol. 5, pp. 33-36, 2018.

[73] T. A. Olds, S. E. Karcher, K. W. Kriegsman, *et al.*, "Oxidation and anion lattice defect signatures of hypostoichiometric lanthanide-doped $UO_2$", *Journal of Nuclear Materials*, vol. 530, p. 151959, 2020.

| FIRMANTE | NOMBRE | FECHA | NOTAS |
|---|---|---|---|
| **FIRMANTE[1]** | **MARIA NIEVES RODRIGUEZ VILLAGRA** | **16/01/2025 14:17 \| Sin acción específica** | |
| **FIRMANTE[2]** | **JONE MIREN ELORRIETA BAIGORRI** | **16/01/2025 14:32 \| Sin acción específica** | |
| **FIRMANTE[3]** | **M.SOLEDAD FERNANDEZ FERNANDEZ** | **17/01/2025 11:36 \| Sin acción específica** | |
| **FIRMANTE[4]** | **ENRIQUE MIGUEL GONZALEZ ROMERO** | **17/01/2025 11:57 \| Sin acción específica** | |